Effects of confinements on morphology of $In_xGa_{1-x}As$ thin film grown on sub-micron patterned GaAs substrate: elastoplastic phase field model

M. Arjmand[1], J. Deng[2], N. Swaminathan[3], D. Morgan[1,2], and I. Szlufarska[1,2]

[1]*Department of Engineering Physics, University of Wisconsin – Madison, Madison, 53706, USA*

[2]*Department of Materials Science and Engineering, University of Wisconsin – Madison, Madison, 53706, USA*

[3]*Department of Mechanical Engineering, Indian Institute of Technology, Madras, India*

An elastoplastic phase field model is developed to investigate the role of lateral confinement on morphology of thin films grown heteroepitaxially on patterned substrates. Parameters of the model are chosen to represent $In_xGa_{1-x}As$ thin films growing on GaAs patterned with SiO_2. We determined the effect of misfit strain on morphology of thin films grown in 0.5μm patterns with non-uniform deposition flux. Growth of islands inside patterns can be controlled by non-uniformity of deposition flux, misfit strain between film and the substrate, and also strain energy relaxation due to plastic deformation. Our results show that the evolution of island morphology depends non-monotonically on indium content and associated misfit strain due to coupling between the plastic relaxation and the confinements effects. Low indium concentration (0-40%) causes formation of instabilities with relatively long wavelengths across the width of the pattern. Low surface diffusion (due to low indium concentration) and fewer islands across the pattern (due to small misfit strain) lead to formation and growth of islands near the walls driven by overflow flux. Further increase in indium concentration (40-75%) increases the lattice mismatch and surface diffusivity of the film, and also activates plastic deformation mechanism, which leads to coalescence of islands usually away from the edges. By further increasing the indium concentration (up to 100%), plastic deformation relaxes most of the strain energy density of the film, which prevents formation of instabilities in the film. Hence, in this case islands are only formed near the walls.

I. INTRODUCTION

Growth of semiconductors on patterned substrates provides an effective approach to fabricate ordered surface structures such as quantum-dots[1], nano-rods[2] and nano-rings[3]. These nano-structures are used for a number of different applications, including solar cells, sensors, electronic and photonic devices[4]. Advancements in patterning techniques, e.g., self-assembly processes[5], lithographic methods[6-8], scanning probe techniques[9] and block copolymer methods[10], make it now possible to prepare large-scale arrays with a precisely tailored shape, size, and crystallographic orientation[4].

Of particular interest to this study is the use of patterned substrates to grow III-V semiconductor thin films. Multiple experimental studies have been reported in this area. For instance, Jha *et al.*[11] used block copolymer lithography (BCL) to pattern GaAs and to grow GaSb. Brammertz *et al.*[12] selectively grew GaAs films on Ge using SiO_2 mask layers. Martin-Sanchez *et al.*[13] combined atomic force microscopy and local oxidation nanolithography to grow InAs quantum dots on GaAs substrate. Elarde *et al.*[14] studied preferential sites for quantum dots growth of InGaAs/GaAs system using the selective area epitaxy method. Hoshii *et al.*[15] demonstrated that micro selective area growth is an effective way to increase the quality of crystal InGaAs on Si substrates using SiO_2 patterns. They showed that one could control the nucleation process and potentially reduce the number of InGaAs nuclei on Si substrate by using very small area regions of Si. Ganesan *et al.* [16] used SiO_2 patterns made by lateral epitaxial growth to study growth of InAs film on GaAs substrates using metalorganic chemical vapor deposition method. One of the key observations from these studies is that patterns can be utilized to control nucleation and growth of islands, as well as their crystallographic orientations. For example, in the study of Ganesan *et al*[16], who used strip-shaped patterns (trenches), it was found that trenches of different sizes can provide an effective way to control the morphology of the islands. Specifically, for patterns that are approximately 0.6 μm wide, scattered islands were able to find and coalesce with each other[16], which can lead to reduction in the number of nuclei and an improvement in crystal quality.[15] The growth of islands near walls in patterned morphologies has been attributed to the effects of overflow growth, which means that an additional material is deposited near the walls because it does not stick to the patterned mask and flows down along the pattern walls into the trenches[17]. However, it is not clear how this contribution from overflow flux interacts with the effects of surface diffusion of the film, lattice mismatch between the film and the substrate, and plastic relaxation to produce the final morphology of the film.

Contributions to energy during heteroepitaxial growth of thin films on patterned substrates come from strain energy due to the lattice mismatch between the film and the substrate, surface energy of the film, and interfacial energy between the film and the walls of the patterns. Morphology evolution (formation of islands) and plastic deformation due to formation of dislocations are two mechanisms that can relax the energy during such growth. Two main mechanisms have been proposed to lead to formation of islands: surface instability due to strain energy[18] and dewetting[18, 19]. These mechanisms may be active

simultaneously during heteroepitaxial growth[20]. Surface instability, which is caused by non-hydrostatic stress, is referred to as the Asaro-Tiller-Grinfeld-Srolovitz (ATGS) instability[21-23]. In this case, surface morphology is determined by the competition between strain energy due to lattice mismatch and surface energy, which competition may lead to formation of islands. These islands can subsequently coalesce and grow. On the other hand, the dewetting mechanism is driven by competition among surface energies of the film and the substrate and their interfacial energy. In this paper, we assume there is always a wetting layer between the film and the substrate and therefore our focus will be on the effects of the competition between strain and surface energy of the film. An alternative strain relief method is formation of misfit dislocations, which usually happens when the film thickness is above a critical limit. Dislocations are mostly formed at film-substrate interface and can cause deterioration of electronic properties of the film. Several theoretical and experimental studies[24-28] have suggested that both morphological evolutions and plastic deformation take place in films above the critical thickness.

Simulations provide a powerful approach that is complementary to experiments and that allows a systematic investigation of the various factors that impact morphological evolution of heteroepitaxially grown films. A range of computational tools has been previously employed to address different aspects of such growth. These tools include *ab inito* methods [29], molecular dynamics based on classical force fields [30], kinetic Monte-Carlo [31] and continuum models, where the latter ones can be divided into sharp interface [32, 33] and diffuse interface models [34, 35]. In conventional continuum modeling approaches to microstructural evolution, the interfaces between different phases (e.g., the film/vapor and film/substrate interfaces) are considered to be sharp and consequently it is necessary to define a multi-domain structure to model these systems. For each domain one set of differential equations is being solved while the constitutive equations and flux boundary conditions have to be satisfied at the interfaces. Hence one needs to track explicitly each moving interface, which can be numerically challenging for morphologically complex interfaces and for multiphase systems (which contain many interfaces)[35, 36].

Each of the aforementioned modeling approaches has its own advantages. Of particular interest to the current study are continuum models since they enable simulations of growth on the experimental time and length scales [37-39]. One example of using continuum approaches to study growth is the study of Tu and Tersoff [39], who modeled the effect of intermixing of the deposited material and the substrate on the planar

growth of thin films. The critical thickness predicted by their model has a similar dependence on misfit strain as seen experimentally. The same authors have also used sharp interface models to investigate island formation and evolution of heteroepitaxial systems[38]. They observed morphological changes and alloy intermixing as active methods to reduce the free energy of the system. It was also found that there is a strong coupling between morphological and compositional evolutions due to surface diffusivity, which is the main mass diffusion mechanism implemented in the model in Refs[38, 39].

Among diffuse interface approaches, phase field modeling has emerged in recent years as an effective numerical tool for studies of film growth. In a phase field model one can capture both the thermodynamic effects (e.g., the elastic strain energy and the thermodynamic stability of a given phase) and the kinetic effects (e.g., the deposition flux and diffusion) on growth[35, 40]. Phase field models have already been successfully used to study problems related to the ATGS instability [32, 41-45]. For instance, Eggleston *et al.* [34] developed a phase field model to investigate the growth of thin films on non-patterned and patterned substrates. The patterned systems consisted of long and narrow mesas deposited on the substrate. Simulations showed formation of wavelike islands due to surface instability of films during the growth. They also showed that the presence of mesas causes formation of highly ordered arrays of nanocrystalline islands. Interestingly, including anisotropy of the surface energy of the film led to a faster occurrence of instability on the film surface. This phenomenon reduced the distance over which instability wave travels, causing a reduction in the island ordering. In a different study Wise *et al.* [46] investigated the effects of an inclusion buried in the substrate on the morphology of the film during growth. The authors reported the same waviness on the surface as observed by Eggleston *et al.* [34]. It was found that the embedded particle localized the growing islands, leading to the idea that strain patterning could be used to increase the ordering of islands. In addition, Wise *et al.* [37] considered the effects of strain energy due to compositional strain and surface energy on the morphology of binary alloys. Simulations showed that there is a competition between the surface energy and compositional strain energy, which leads to alignment of segregated phases with respect to the film surface. This alignment can be either parallel or perpendicular to the surface, depending on the simulation conditions. For large enough compositional strain, phase separation is controlled by strain energy and alignment of phases perpendicular to the free surface is more favorable. For smaller compositional strain, surface energy dominates the morphological evolution, leading

to a parallel alignment of the separated phases with respect to the surface. The ATGS surface instability has been also studied by Boyne *et al.*[20], who used phase field to simulate heteroepitaxial morphological evolution of gadolinia-doped ceria films deposited on yttria-stabilized zirconia. The authors considered the effects of confinement (patches) present on the substrate. They assumed a constant misfit strain due to lattice mismatch throughout the film. Similarly to the previously discussed results, Boyne *et al.* [20] reported development of wavelike ordering in the stress driven instability on the surface of the thin film surface. Instabilities were initiated next to the surface patches and it was found that when a misfit stress exists in the substrate and in the patches, instability starts more quickly than in the case of stress-free patches. However, Boyne *et al.* [20] did not study the kinetic effect associated with the deposition flux and how this deposition flux couples to diffusion. Also the effect of relaxation associated with plastic deformation was not investigated in their model.

In crystalline materials, plastic deformation is mainly due to formation of dislocations. Hence, several studies have been reported that couple dislocation plasticity to the phase field formation. Dislocations can be introduced into the model either explicitly or through constitutive elasto-plastic equations. Explicit models treat dislocations as continuous fields on each slip system and couple these fields to phase field variables. The most important advantage of this method is that it inherently includes interactions between dislocations. An example of this approach was reported in 2001 by Wang *et al.*[47, 48], who studied multi-dislocation system in elastically anisotropic crystals. Later on, Hataaja *et al.*[49] introduced phase field formulation coupled with dislocations as a model for non-equilibrium multiphase systems to simulate the dynamics of lattice-mismatched heteroepitaxial films. The authors investigated how dislocations can compete with surface instability to relief strain during the film growth. Hataaja *et al.*[50] later developed their model to include the effects of nucleation, interactions and dynamics of dislocation. Wang *et al.*[51] added an extension to the phase field microelasticity to study the dislocation dynamics near a free surface in heteroepitaxial thin films. However, there are a couple of drawbacks associated with the approach of studying dislocations explicitly. Firstly, one needs sub nanometer grid size to model the dislocation cores, which limits the total size of the simulation domain. Consequently, while explicit modeling of dislocations has been implemented before studying growth of heteroepitaxial thin films, this has been done only for non-patterned surfaces. Secondly, different mechanisms for dislocations (other than glide) have not been

accounted for yet within phase field models, and this is still an active area of research[52]. Another approach is to model dislocations implicitly by coupling elasto-plastic constitutive equations to the phase field model through plastic strain field. This approach does not require very fine grid points and therefore is amenable to simulating larger simulation domains with nanopatterns. Flow rule and hardening law in the form of ordinary differential equations need to be solved in addition to equilibrium, constitutive and compatibility equations, and one needs to add a yield condition to the model. This approach was used by Guo *et al.*[53] who coupled plasticity to a phase field model to study the stress distribution around defects, such as cracks and holes. Gaubert *et al.*[54] developed an elasto-visco-plastic model to study microstructural evolution during a creep loading in superalloys. Cottura *et al.*[52] developed a size dependent viscoplastic phase field model to study the rafting of the microstructures. However, this kind of approach has not previously been applied to study heteroepitaxial growth on patterned substrates. Since we are not interested in lower length scale information about dislocation structures and also because of numerical efficiency of this type of method, we choose it for our investigation. Specifically, here we developed a phase field model coupled with elastoplasticity equations to determine how surface patterning, misfit strain, and plastic relaxation affect morphology of thin films. In order to be consistent with typical experimental conditions, we include in the model a biased deposition, with statistical non-uniformity of the deposition flux expected for patterned substrates[17], and high interfacial energy between the film and the walls of the patterns (non-wetting conditions). One of the key questions that we answer with these simulations is under what conditions islands can nucleate and grown near the edges of the patterns. Such a growth pattern is attractive since it leads to a more uniform island size distribution and a more uniform crystallographic orientation of the islands[16]. Another important question we answer is under what circumstances small islands coalesce to form a single island across the pattern. Again, such single island structures are preferred as they can decrease the density of defects[15, 55]. The parameters in our study are chosen so that the film has the effective properties of $In_xGa_{1-x}As$, the substrate the properties of GaAs, and the pattern walls the properties of SiO_2.

II. ELASTOPLASTIC PHASE FIELD MODEL

In this section we report governing equations, boundary conditions, and the simulation parameters used to model heteroepitaxial growth of thin films under the conditions of lateral confinements due to surface

patterning. We will investigate the effects of misfit strain and plastic deformations on morphology of the thin film grown in 0.5 μm-wide pattern under effects of non-uniform overflow flux and at a constant temperature. Schematic cross-sectional view of the patterned substrate with overflow deposition flux is shown in Fig. 1(a). As shown in Fig. 1(b), the model consists of the substrate (orange), walls of the confining pattern (dark blue), the gas phase (light blue) and the film (red). We treat each of these sections as a one-component system (one phase), with effective properties of GaAs (for the substrate), SiO_2 (for the walls) and $In_xGa_{1-x}As$ (for the film). The concentration of the growing film varies between $c = 0$ (representing the vapor phase and shown in light blue) to $c = 1$ (representing the solid phase and shown in red). In our simulations, we treat the film as one phase and do not allow for phase separation. This assumption is consistent with experimental observation of no phase separation in InGaAs grown on GaAs[16]. The wall and the substrate are considered to be in the solid phase with concentrations equal to 1. Here, we assume that there is always a wetting layer (called a boundary-layer[34]) on the substrate. Therefore, the substrate is never exposed to the gas phase and the interface between the film and the substrate does not evolve with time. In addition, we assume that the main mass transport mechanism in the film is via surface diffusion, which occurs around the film-vapor interface. This is a common assumption for heteroepitaxial growth of thin films[34]. Bulk diffusion is ignored in the film, the substrate, and the walls and there is no mass transport between these three regions.

In many experiments, patterns have the form of long strips[15, 16]. In our two-dimensional simulations we represent such experiments by assuming plain strain conditions. Specifically, the pattern wall has an infinite length along the *z* direction (into the plane of Fig. 1). Deposition flux has a random perturbation of ±5% in the flux magnitude introduced at each grid point across the width of pattern under both uniform and biased deposition conditions to represent the noise in deposition process [34]. Random numbers are drawn from a uniform distribution. This randomness also provides the perturbation needed to initiate surface instability [34].

We model the film growth using the phase field method combined with elastoplasticity equations. Following Cahn and Hilliard[56] and Allen and Cahn[57] equations, the total free energy F of the system can be written in the following functional form

$$F = \int_\Omega \left(f(c) + W(c) + \frac{\varepsilon^2}{2} |\nabla c|^2 \right) \mathrm{d}\Omega + \oint_{B_1} f_s(c)\, \mathrm{d}l \qquad (1)$$

The above total free energy of the system consists of two integrals, and each of them is discussed below in detail. In the first integral on the right hand side (rhs) of Eq. (1), Ω represents the cross-sectional area of the entire system, c is the concentration (density). ε^2 is the gradient energy coefficient. Following the formulation developed by Egglestone *et. al*[34], anisotropic interfacial energy between film and gas is defined as

$$\varepsilon(\theta) = \varepsilon_0(1 + \varepsilon_4\cos(4\theta)) \quad (2)$$

where ε_0 is the gradient energy constant, θ is the angle between the normal to the contour of constant concentration and the x axis and ε_4 is a constant between 0 to 1, which determines the degree of anisotropy. The variation of ε_4 with distance from the substrate has been adopted from Egglestone *et. al*[34].

In the first integral on the rhs of Eq. (1), f is the free energy density and it is a function of concentration. We use a double-well potential, f_1, for the free energy density function in the film. In the substrate and the walls, we use a single-well potential, f_2, to restrict their evolution [20]. Specifically,

$$f_1(c) = \frac{1}{4}w_0c^2(1-c)^2 \quad (3)$$

$$f_2(c) = \frac{1}{4}w_0(1-c)^2 \quad (4)$$

where w_0 represents the barrier height of the single and double-well functions representing the local free energy density. Symbol W in Eq. (1) has contributions from elastic and plastic energy densities, which are defined as

$$W(c) = W^{el}(c) + W^{pl}(c) \quad (5)$$

where $W(c)$ is the total work, $W^{pl}(c)$ is the plastic work

$$W^{pl}(c) = \int_0^{e^{pl}} \sigma_{ij}\, de_{ij}{}^{pl} \quad (6)$$

$e_{ij}{}^{pl}$ is plastic strain tensor and σ_{ij} is the Cauchy stress tensor. $W^{el}(c)$ is the elastic work given as

$$W^{el}(c) = \frac{1}{2}\sigma_{ij}\, e_{ij}{}^{el} \quad (7)$$

where $e_{ij}{}^{el}$ is an elastic strain tensor which can be given as

$$e_{ij}{}^{el} = e_{ij}{}^{tot} - e_{ij}{}^{*} - e_{ij}{}^{pl} \quad (8)$$

where $e_{ij}{}^{tot}$ is the total strain and $e_{ij}{}^{*}$ is the eigenstrain associated with the difference between lattice parameters of the film and the substrate. Assuming a linear strain displacement relationship, the total strain can be written as

$$e_{ij}{}^{tot} = \frac{1}{2}\left(u_{i,j} + u_{j,i}\right) \quad (9)$$

where $u_{i,j}$ is the derivative in the *j* direction of the displacement in *i* direction. Total strain is calculated by solving the mechanical equilibrium (Cauchy-Navier) equation

$$\frac{\partial \sigma_{ij}}{\partial x_j} = 0 \quad (10)$$

Following Egglestone *et al.*[34] eigenstrain in our model is defined as

$$e_{ij}{}^{*} = \frac{1}{2}\,\widehat{e_f}\,\left(1 + f_{BL}(y)\right)\delta_{ij} \quad (11)$$

where δ_{ij} is kreneckar delta and f_{BL} is the boundary layer function of the same form as in Ref. [34] $\widehat{e_f}$ is the lattice mismatch which is given by

$$\widehat{e_f} = \frac{a_{film} - a_{substrate}}{a_{substrate}} \quad (12)$$

To find the plastic strain tensor we need to define a yield function, a flow rule and a hardening rule. Here, we use *J2* plasticity (Von-Mises criteria) with the yield function

$$F\left(\sigma_{ij}, \sigma_Y\right) = \sigma_{mises} - \sigma_Y \leq 0 \quad (13)$$

where *F* is the yield function, σ_Y is the current yield stress, and σ_{mises} is the Von-Misses stress. For isotropic hardening, flow rule is given by

$$\dot{e}_{ij}{}^{pl} = \lambda \frac{\partial F\left(\sigma_{ij}, \sigma_Y\right)}{\partial \sigma_{ij}} \quad (14)$$

where $\dot{e}_{ij}{}^{pl}$ is plastic strain rate and λ is plastic multiplier which is a positive number. For the film and the substrate materials we assume a linear work hardening, which can be written mathematically as

$$\sigma_Y = \sigma_{Y0} + \sigma_h \quad (15)$$

where σ_{Y0} is the initial yield stress and σ_h is the work hardening function

$$\sigma_h = E_t * e^{pl} \quad (16)$$

where E_t is tangential Young's modulus. This value was measured for InGaAs layers to be approximately 20% of the Young's modulus[58] of InGaAs. Since E_t was not measured for the entire range of compositions, we assume this value to be a reasonable approximation for all compositions we study.

The second integral on the rhs of Eq. (1) corresponds to surface and interfacial energies on B_1, where B_1 represents the interface between the film and the walls (b6 and b7 in Fig. 1(b)). f_s stands for the difference between interfacial energy densities for the film/wall and vapor/wall interfaces. There is a

convenient way to include the term f_s into the model, which was first introduced by Cahn [59] and later used by Wise *et al.*[37, 60] . Specifically,

$$f_s(c) = s_1 c \tag{17}$$

where s_1 is a positive constant. Eq.(17) assumes that f_s is linearly dependent on concentration of the nearby phase. Higher values of s_1 correspond to more non-wetting conditions at the interface. The approximation given in Eq.(17) has been shown to be in agreement with the nearest-neighbor bond counting approximation [37, 60], in which the surface/interfacial energy is calculated based on energy contributions from broken bonds at that surface/interface. To our knowledge, the interfacial energy between $In_xGa_{1-x}As$ film and the SiO_2 wall has not been measured experimentally. However, experimental observations [16] imply non-wetting conditions at such interface. Therefore in our simulations we will use s_1 = 0.03, which corresponds to an interfacial energy that is high enough to produce non-wetting conditions in our simulations. The interfacial energy between $In_xGa_{1-x}As$ film and the GaAs substrate is assumed to be negligible. The interfacial energy between $In_xGa_{1-x}As$ film and the vapor will be defined later.

The different boundaries present in our simulations are defined in Fig. 1(b). We use the displacement and/or traction vectors to define boundary conditions. We assume that the displacements vanish at the lower boundary of the substrate (b1). The outer boundaries, b2 and b3, are also kept fixed (zero displacements) while the top boundary of the gas phase region (b4) is assumed to be traction free. Since the growing film is very thin, we assume that the traction vector at b5 is also zero. The displacement and the traction vectors are continuous across the boundary b5. The traction, which the elastic walls exert on the film, is proportional to the displacement along the *x* direction of the boundaries b6 and b7. In addition, the traction vector is continuous across the wall/film boundaries, b6 and b7. The *x* component of displacement vector u_x is continuous across the boundaries b6 and b7, while the *y* component u_y of displacement field is not in order to enable the film to climb up the wall in case it is favorable.

In our model concentration (*c*) is a conserved field variable. Concentration evolves according to the mass conservation equation

$$\frac{\partial c}{\partial t} = -\nabla . J + J_d n_y \tag{18}$$

where *J* is the density flux, which can be related to the gradient of variational derivative of the free energy density functional as

$$J = -M(c)\nabla\frac{\delta F}{\delta c} = -M(c)\nabla\left(\frac{\partial f}{\partial c} + \frac{\partial W^{el}}{\partial c} + \frac{\partial W^{pl}}{\partial c} - \nabla.(\varepsilon^2\nabla c) + \frac{\partial}{\partial x}(\varepsilon\frac{d\varepsilon}{d\theta}\frac{\partial c}{\partial y}) - \frac{\partial}{\partial y}(\varepsilon\frac{d\varepsilon}{d\theta}\frac{\partial c}{\partial x})\right) \quad (19)$$

where $\frac{\delta}{\delta c}$ is variational derivative. The plasticity driving force on concentration field is $\frac{\partial W^{pl}}{\partial c}$. Since the majority of the plastic work in crystalline systems is released as heat, we assume that the effect of plastic work as driving force for evolution of the concentration filed is negligible. $M(c)$ is the mobility, which depends on the concentration in the following way

$$M(c) = M_s c^2(1-c)^2 \quad (20)$$

where M_s is the surface mobility. In Eq.(18), J_d is the deposition flux and n_y is the vertical component of the surface normal. J_d is defined as[34]

$$J_d = V_d A_0\, c^2(1-c)^2\, R_0 \quad (21)$$

where V_d is the surface velocity (growth rate) due to deposition, R_0 is a random number between 0.95 to 1.05, and $A_0 = \frac{6}{\delta}$, where δ is the interfacial thickness. Combining Eqs. (18) and (19), one can derive the following Cahn-Hilliard equation [61]

$$\frac{\partial c}{\partial t} = \nabla.\left[M(c)\nabla\left(\frac{\partial f}{\partial c} + \frac{\partial W^{el}}{\partial c} - \nabla.(\varepsilon^2\nabla c) + \frac{\partial}{\partial x}(\varepsilon\frac{d\varepsilon}{d\theta}\frac{\partial c}{\partial y}) - \frac{\partial}{\partial y}(\varepsilon\frac{d\varepsilon}{d\theta}\frac{\partial c}{\partial x})\right)\right] + J_d n_y \quad (22)$$

Note that in this work, the coupling between plasticity and microstructure evolution is only through the elastic driving force, which is an approach often taken in the literature[54].

As shown in Eq.(1) and Eq.(19), our phase field model is coupled to the elastic energy of the system. This coupling is implemented by solving Cauchy-Navier equations (Eq.(10)) in two dimensions simultaneously with the Cahn-Hilliard equation (Eq. (22)) to find the displacement and concentration fields at each time step of the simulation. Since we have a 2-D model, all energies in the model are defined per unit of length along the *z* direction. We wrote our phase field code using the commercial software, COMSOL, which solves systems of partial differential equations using finite element method. The total dimensions of the model are 500×180 grid points, with more grid points along the *x* direction. We use a non-uniform mesh along the *y* direction with a more refined mesh size (~1 Å) near the substrate and coarser mesh size (~1 nm) in the gas phase away from the substrate.

In the model we assume homogenous and cubic elastic constants for the film and the substrate while isotropic elastic constants has been used for the walls. The elastic constants, yield strength, surface energy, diffusion coefficient and growth conditions for different indium concentrations are listed in Table I.

Table I. Elastic constants, yield strength, surface energy, diffusion coefficient and growth conditions for different indium concentrations.

Input parameters	Substrate (GaAs)	Film ($In_xGa_{1-x}As$)				
Concentration x	0	0.1	0.25	0.5	0.75	1
C_{11} (GPa)	118.8 [62]	115.2	109.9	101.1	92.2	83.4 [62]
C_{12} (GPa)	53.4 [62]	52.6	51.4	49.4	42.5	45.4 [62]
C_{44} (GPa)	59.6 [62]	57.6	54.6	49.5	44.5	39.5 [62]
Yield strength σ_{Y0} (GPa)	5 [58]	5.5 [58]	5.5 [58]	4.5 [58]	3 [58]	2.5 [58]
Surface energy γ (J m^{-2})	0.714 [62]	0.712	0.710	0.706	0.703	0.699 [62]
Gradient energy coefficient ${\varepsilon_0}^2$ (nJ m^{-1})	-	2.137	2.131	2.119	2.108	2.097
Lattice mismatch (%)	0	0.71	1.79	3.58	5.37	7.17
Diffusion coefficient D_0(cm^2 s^{-1})	1×10^{-7} [63]	1.9×10^{-7}	3.25×10^{-7}	5.5×10^{-7}	7.75×10^{-7}	1×10^{-6} [64]

Elastic constants, surface energy and diffusion coefficients for pure GaAs and InAs are found from Refs[62-64], as indicated in Table I. We use a linear interpolation between compositions x = 0 and x = 1 to find the properties for $In_xGa_{1-x}As$ for different indium concentrations. The yield stress of InGaAs, which is an input parameter to our model, is extracted from Korte *et al.*[58] The interfacial energy γ and interfacial thickness δ are related to gradient energy coefficient ${\varepsilon_0}^2$ and the barrier height of the double-well function w_0 through $\gamma = \frac{\varepsilon_0}{6}\sqrt{\frac{w_0}{2}}$ and $\delta = \varepsilon_0\sqrt{\frac{2}{w_0}}$ (see for instance Ref. [34]). The interfacial thickness is assumed to be about 5 Å and the grid size near the substrate is about 1 Å. From the expression for the interfacial thickness and interfacial energy, we calculate w_0 to be 1.75×10^9 J m^{-3}. To describe anisotropic interfacial energy, we accepted the formulation developed by Egglestone *et al.*[34], where gradient energy coefficient ${\varepsilon_0}^2$ is calculated and shown in Table I for different indium concentrations. The anisotropic gradient energy coefficient is assumed to vary with thickness as derived in Egglestone *et al.*[34] The surface mobility M_s depends on surface diffusion coefficient D_0 through $D_0 = M_s RT$, where T is temperature and R is gas constant. M_s is assumed to be 4.36×10^{-18} m^5 J^{-1} s^{-1} for InAs and 3.54×10^{-20} m^5 J^{-1} s^{-1} for GaAs, which corresponds to surface diffusivity of 1×10^{-6} cm^2 s^{-1} and 1×10^{-7} cm^2 s^{-1}, respectively [62, 64]. Growth

temperature T is set to 650 ℃. Growth rate is assumed to be 1 nm/s. The simulation parameters are normalized in the following way. We use l^* as the characteristic length (taken to be 1 nm), e^* as the characteristic energy density (taken to be 10^{10} J m^{-3}) and t^* as the characteristic time (chosen to be 10^{-8} s). Using these dimensionless parameters, we define other dimensionless quantities, which are free energy density ($f^* = \frac{f}{e^*}$), elastic moduli ($C_{ij}^* = \frac{C_{ij}}{e^*}$), strain energy density ($W^* = \frac{W}{e^*}$), gradient energy coefficient ($\varepsilon^{*2} = \frac{\varepsilon^2}{l^{*2}.e^*}$), mobility ($M^* = \frac{M_s t^*.e^*}{l^{*2}}$) and deposition flux rate ($J_d{}^* = t^*.\ J_d$). We can also write a dimensionless form of the Cahn-Hilliard equation

$$\frac{\partial c}{\partial \hat{t}} = \hat{\nabla}.\left[M^*(c)\hat{\nabla}\left(\frac{\partial f^*}{\partial c} + \frac{\partial W^{el^*}}{\partial c} - \hat{\nabla}.(\varepsilon^{*2}\hat{\nabla}c) + \frac{\partial}{\partial \hat{x}}(\varepsilon^* \frac{d\varepsilon^*}{d\theta}\frac{\partial c}{\partial \hat{y}}) - \frac{\partial}{\partial \hat{y}}(\varepsilon^* \frac{d\varepsilon^*}{d\theta}\frac{\partial c}{\partial \hat{x}})\right)\right] + J^*{}_d n_y \qquad (23)$$

where the $\hat{\nabla}$ symbol represents a gradient with respect to non-dimensional variables $\hat{x}$ and $\hat{y}$.

Simulations are performed for the total time of 5×10^7, 1×10^8 and 5×10^8 simulation steps Δt, where Δt = 10^{-8} s. We report time in seconds, but one can convert seconds to time steps by dividing the simulation time by Δt. The total time of the simulations was chosen so that the total energy variation between last two time steps is less than 1×10^{-6} percent of the total energy, indicating very small change in the morphology.

III. RESULTS

We report results of phase field simulations of heteroepitaxial growth of thin films on patterned substrates coupled with elastoplastic governing equations, with parameters corresponding to the $In_xGa_{1-x}As$/GaAs systems with SiO_2 patterns. Our goal is to determine how patterns control the morphology of islands during growth. More specifically, we identify conditions leading to the island growth near the walls of the SiO_2 patterns and conditions under which a single island grows away from the walls. We investigate how the morphology of the growing film is affected by the lattice mismatch between the film and the substrate and also we study the role of plastic relaxation in the film on morphology. Our model includes a biased deposition flux and high interfacial energy between the film and confining walls of the pattern, to emulate experimental conditions. Although plastic relaxation is allowed in our model for all In concentrations in the $In_xGa_{1-x}As$/GaAs alloy, we found that it occurs only for In concentrations higher than 0.4. Therefore we break up the discussion of our results into the low- (<0.4) and high- (>0.4) In concentration regimes.

A. Low indium concentration $In_xGa_{1-x}As/GaAs$ (x < 0.4)

Here we investigate the effect of misfit strain on the morphology of the islands across the pattern. It is of particular interest to know under what condition islands coalesce to make a single nucleus and when they form multiple nuclei. For instance, as discussed in the introduction, experimental observations have shown the existence of the overflow flux near the walls [17] and the question arises whether this overflow flux will always lead to formation of islands near the edges of the patterns or whether it competes with other equally strong effects on film morphology.

First we study growth of $In_{0.1}Ga_{0.9}As$ film on GaAs substrate with SiO_2 confining walls. Our model includes the effect of the overflow flux, which means that effectively there is a higher local deposition of material near the walls. Under experimental conditions, deposition flux is actually uniform throughout the entire patterned sample. However, since the deposited material does not form strong bonds with the SiO_2 mask, it does not grow on top of the mask. This behavior was demonstrated experimentally for example during InAs growth on patterned GaAs substrate, where the deposited material was growing in the trenches only[16, 17]. As a result, the material initially deposited on SiO_2 flows down the walls toward the substrate and the film growing on top of it. This idea is schematically shown in Fig. 1(a). To estimate the flux near the walls, we assume the trenches are equally spaced and separated by 0.5 μm-wide SiO_2 mask. Under these conditions, the overflow material deposited near each wall is equal to half of the material deposited on top of the SiO_2 mask. We assume that this additional flux is spread over a distance of two finite element mesh grids in our simulations, which corresponds to a physical distance of 2 nm. The results of phase field simulations at different times during for growth with x = 0.1 In concentration are shown in Fig. 2. This low indium concentration (with a corresponding lattice mismatch of 0.71 %) does not cause any instability in the initial flat film, except for near the edges due to unfavorable interfacial energy between the film and the walls as shown in Figs. 2(a)-(b). During further deposition of material, we observe only two relatively symmetric islands that are wide enough to spread between the edge and the center of the pattern. The wide spreading of the islands is possible due to the relatively low cost in the strain energy. The ratio of strain energy to total energy (which consists of surface and strain energies) after 10^{-5} s is 1.7% while this ratio increases to 7.8% after 5 seconds. Strain energy is increased due to deposition of additional strained

material (where strain is caused by lattice mismatch between deposited film and the substrate) while the surface energy is slightly decreased. No plastic relaxation was observed during these simulations. One should note, however, that plastic deformation might occur at later stages of growth when the islands continue to grow and coalesce into a continuous film within the trench.

The results of simulation for $In_{0.25}Ga_{0.75}As/GaAs$ are presented in Fig. 3. Except for the parameters that depend on In concentration (see Table 1), such as elastic properties, yield strength and surface diffusion coefficient, all other parameters are kept the same as the results for $In_{0.1}Ga_{0.75}As/GaAs$ reported in Fig. 2. Starting from a flat thin film, we find that perturbations in the growing film first form near the walls as shown in Figs. 3(a)-(b). The same phenomenon was reported by Boyne *et al.*[20] who studied heteroepitaxial growth of gadolinia-doped ceria on yttria-stabilized zirconia with patches (confinement) present on the substrate. After 0.1 s, perturbations due to ATGS instabilities are extended throughout the entire trench (see Fig. 3(c)). The critical wavelength expected based on the linear elasticity theory for infinite films[21] is 84 nm, while the wavelength measured in our simulation is 91 nm. This difference can be attributed to the effect of surface patterning, since the width of the pattern needs to accommodate an integer number of wave peaks and valleys. Since there is a wetting layer on the substrate, dewetting does not play any role in our simulations. In Fig. 3(d), one can see that small islands are formed due to the coalescence of surface instabilities. Biased deposition flux causes faster growth rate of islands near the walls and once these islands are large enough, they absorb other small islands as shown in Fig. 3 (e). These two islands keep growing as long as we deposit the material as demonstrated in Fig. 3(f). During the growth, strain energy of the system increases from 4.41×10^{-8} J/m after 10^{-5} s to 12.86×10^{-8} J/m after 5 s due to the deposition of additional strained material. Relatively slow surface diffusion (as compared to the deposition flux) combined with the effects of biased (overflow) flux are the most important reasons preventing coalescence of the two islands into a single island. It is easy to see that the islands in Fig. 3(f) for 0.25 In concentration have a similar size (length: ~130 nm, height: ~38 nm) and that the length of each island is much smaller than length of islands formed in the case of concentration x = 0.1 In concentration shown in Fig. 2(d) (length: ~250 nm, height: ~25 nm). Comparing the size of islands in these two cases shows that alloys with higher In concentration reduce their elastic energy by reducing the contact area with the substrate and by growing taller islands at the expense of increased surface energy. In Fig. 4(a) we plot Von-Mises (effective)

stress in the $In_{0.25}Ga_{0.75}As$/GaAs system after 5 s of growth. We find that due to formation of the ATGS instabilities, stress in the film which was high at the early stages of growth, is now relaxed. The stress is more relaxed near the top of the islands whereas it is still concentrated at the corners of each island (see Fig. 4(a)). Since the yield strength of the material is higher than the effective stress in the simulations, yielding does not take place. It is instructive to consider the different components of stress along the AB line. As shown in Fig. 4(b), all the components of the stress tensor are zero in the gas phase due to zero elastic constants while there are nonzero components of stress present both in the film and the substrate. The shear stress σ_{xy} is zero both in the substrate and the film along the AB line, but we found it to be finite at the corners of the islands. σ_{yy} is tensile everywhere and its magnitude decreases monotonically from 0.3 GPa at the interface between film and the substrate to around zero near the top of the island. The most important component of the stress, σ_{xx}, is tensile in the substrate but it suddenly becomes compressive in the film. By moving away from the film-substrate interface, σ_{xx} becomes less compressive until it becomes slightly tensile at the top of the island. The presence of tensile stress at the top of the island has been reported in the literature[65-67]. Von Mises stress has its largest magnitude (about 1.8 GPa) at the film-substrate interface while it decreases to 1.6 GPa at the top of the islands and suddenly drops to zero in the gas phase. The variation of strain components along AB line is plotted in Fig. 4(c). The eigenstrain is zero in the substrate and also in the gas phase, while it has a constant value across the film. Elastic strain ε_{xx} on the other hand, changes from compressive at the film-substrate interface to tensile at the top of the island. As expected, the total strain is always a sum of elastic strain and eigenstrain.

Analysis of the above results for two different low In concentrations shows that biased deposition plays an important role in formation of islands near the walls. For both concentrations, only elastic relaxation was present during growth. The effects of plastic relaxation on film morphology (present in films with higher In concentrations) are discussed in the next section.

B. High indium concentration $In_xGa_{1-x}As$ ($x > 0.4$)

We now investigate the effect of further increase of In concentration on the morphology of a heteroepitaxially grown films. For concentrations of In higher than 0.4 we observe plastic relaxation in our simulations and we investigate the effect of plastic relaxation on the film morphology.

We first study growth of $In_{0.5}Ga_{0.5}As$ on GaAs substrates. Again, all the other parameters that do not depend on In concentration were kept constant in the model. By increasing the indium concentration (x), the lattice mismatch between the film and GaAs substrate increases (see Table 1) and so does the accumulated stress. When the effective stress rises above the yield strength of the film, plastic deformation takes place, which partially relaxes the elastic strain and subsequently reduces strain energy of the film. As discussed in Sec. III-A, for the case of $In_{0.25}Ga_{0.75}As$ (x = 0.25) on GaAs we found that the deposited material formed two islands at the walls (see Fig. 3). For comparison, in Fig. 5, we show the results of growth simulations for $In_{0.5}Ga_{0.5}As$/GaAs (x = 0.5) inside the SiO_2 patterns. Similarly as in the case of x = 0.25, here we find that perturbations initiate at the edges of the trenches near the wall (see Figs. 5(a)-(b)). The ratio of elastic energy to the total energy is 28.8% after 10^{-4} s. This ratio drops to 24.5% after 10^{-3} s due to the formation of instabilities on the surface (Fig. 5(c)), which partially relaxes the strain energy density. These instabilities grow into isolated islands and they are able to coalesce as shown in Figs. 5(d)-(e). This coalescence causes further reduction in the ratio of elastic to total energy to 22% after 10^6 and 21.8% after 0.1 s. In this case, the maximum value of the effective plastic strain is 0.1% while the eigenstrain is about 3.5%. Interestingly, during further deposition, all the islands coalesce and form one big island away from the walls as shown in Fig. 5(f). The plastically deformed region has grown in size at the corners of the large island and the magnitude of the maximum value of plastic strain is 3% (see Fig. 5(g)). Partial relaxation due to plastic deformation leads to a slight decrease in the ratio of elastic to total energy, which is now 21.5% after 0.18 s. Further deposition of strained material increases this ratio again to 26.1% after 1 s (due to deposition of strained material). There are two qualitative differences in the final morphologies of $In_{0.5}Ga_{0.5}As$ as (Fig. 5(f)) and of $In_{0.25}Ga_{0.75}As$ (Fig. 3(f)): (i) There is only one island formed for the case of x = 0.5 whereas there are two islands for x = 0.25; (ii) For x = 0.5 the island forms in the middle of the pattern whereas for x =0.25 the islands form near the edges. Formation of one island instead of two reduces the area of the interface between the strained film and the substrate. For the case of x = 0.5 the driving force for strain relaxation is higher (because of the higher misfit strain). In addition, for x=0.5 surface diffusivity of $In_{0.5}Ga_{0.5}As$ is about 70% higher than surface diffusivity of $In_{0.25}Ga_{0.75}As$. Hence, small islands are able to coalesce before the deposition flux can grow islands near the walls. The effects of high surface diffusivity can also explain the second difference in morphology. Islands across the pattern find each other

and coalesce due to high surface diffusivity. Once the islands grow in size, they cannot easily move since they can only move through surface diffusion of the material. This result demonstrates that overflow flux alone is not enough to grow islands near the edges. It competes with the effect of elastic energy and also plastic strain relaxation.

In Table II, we compare the energetics associated with the growth of $In_{0.25}Ga_{0.75}As$ (x = 0.25), studied Sec. III-A (and plotted in Fig. 3) to the growth of $In_{0.5}Ga_{0.5}As$ (x = 0.5) on GaAs shown in Fig. 5. The first two columns in the table show the energetics for $In_{0.25}Ga_{0.75}As$ at the initial step and after 1 s of simulations. The last two columns of the table show the corresponding energetics for $In_{0.5}Ga_{0.5}As$. Initially, the total energy of $In_{0.25}Ga_{0.75}As$ /GaAs system is 73.74×10^{-8} J/m and the total energy of the $In_{0.5}Ga_{0.5}As$ /GaAs system is 79.88×10^{-8} J/m. After 1 s, the total energy of these systems is 44.72×10^{-8} J/m and 55.74×10^{-8} J/m, respectively. Hence one can see that for the higher indium concentration the reduction of the total energy (30.22%) is slightly smaller than the reduction of 39.35% for lower indium concentration. For both systems, the largest contribution of the total energy comes form surface and interfacial energies. This contribution is 86% for $In_{0.25}Ga_{0.75}As$ /GaAs (x = 0.25) and 73% for $In_{0.5}Ga_{0.5}As$ /GaAs (x = 0.5). Surface and interfacial energies for both cases (x = 0.25 and x = 0.5 In concentration) are very close at the initial and the final simulation time (the difference is smaller than 6%) while relatively large differences are observed in strain energies. Specifically, in $In_{0.25}Ga_{0.75}As$ the strain energy increases from 2.49×10^{-8} J/m at the beginning of simulation to 6.17×10^{-8} J/m after 1 s. The same qualitative trend is also found for $In_{0.5}Ga_{0.5}As$, but with a smaller relative increase. Plastic energy is zero at the beginning for both $In_{0.25}Ga_{0.75}As$/GaAs and $In_{0.5}Ga_{0.5}As$/GaAs systems. After 1 s, this energy remains zero for x = 0.25 system while it is 0.31×10^{-8} J/m for x = 0.5, as shown in Table III.

Table II. Energy comparison between $In_{0.25}Ga_{0.75}As$ and $In_{0.5}Ga_{0.5}As$ thin films grown on GaAs. Surface energy refers to the energy of the film surface in contact with the gas phase. Interface energy refers to the energy between film and the walls.

Composition	$In_{0.25}Ga_{0.75}As$		$In_{0.5}Ga_{0.5}As$	
Time (s)	0	1	0	1
Surface and interface energy (10^{-8} J/m)	71.25	38.54	70.87	41.19
Strain energy (10^{-8} J/m)	2.49	6.17	9.01	14.55
Plastic energy (10^{-8} J/m)	0	0	0	0.31
Total (elastic + plastic + interfacial) energy (10^{-8} J/m)	73.74	44.72	79.88	56.05

To bring further insights into the effect of lattice mismatch and plastic relaxation on film morphology we have simulated growth of alloys with higher In concentrations. For x=0.75, we see trends in morphology that are qualitatively similar to those for x = 0.5 shown in Fig. 5., Specifically, instabilities start near the walls, spread throughout the pattern, islands form and coalesce into a single island in the middle of the pattern. Higher In concentration reduces the wavelength of ATGS instabilities, which is 20 nm for x = 0.75 and 29 nm for x = 0.5 (Fig. 5(c)). Another difference is that for x=0.75, plastic deformation begins in the film early on (at $t = 1\times10^3$) and generally plastic strain is larger. Hence it is instructive to analyze the stress and strain the film. Von Mises stress for $In_{0.75}Ga_{0.25}As/GaAs$ after 0.16 s is shown in Fig. 6(a). The stress in the thin film introduced by lattice mismatch is relaxed both by formation of instabilities and by plastic deformation. In this case, the flow strength in the film increases from the initial value of 3.5 GPa to value of 4.91 GPa at 0.16 s. It is worth pointing out that the GaAs substrate is also allowed to deform plastically. However, the effective stress never reaches that yields strength of 5 GPa and therefore such relaxation does not take place in the substrate. Different components of stress along AB line are plotted in Fig. 6(b). Since the AB line cuts through the middle of an island, shear stress σ_{xy} is zero both in the film and the substrate. σ_{yy} is tensile in substrate but reduces gradually and remains slightly compressive at the top of the island. σ_{xx} is tensile in the substrate with the highest magnitude near the film substrate interface, and it abruptly switches to compressive in the film. In addition, the magnitude of σ_{xx} shows a small drop in the film near the substrate. The same behavior is observed for Von Mises stress. This drop in stress is the result of plastic relaxation and it has not been observed in Fig. 4(b) for a lower In concentration of x = 0.25. Strain components corresponding to the growth stage in Fig. 6(a) are plotted in Fig. 6(c). Similarly to Fig. 4(c), eigenstrain is constant across the film while it remains zero both in the substrate and gas. Plastic strain causes partial relaxation of elastic strain near the film-substrate interface while no plastic deformation occurs by moving away from the interface. Plastic strain remains zero both in the substrate and the gas phase. Elastic strain ε_{xx}, which is partially relaxed near the film-substrate interface, keeps increasing along AB line and it becomes tensile at the top of the island.

Finally, in Fig. 7 we show simulation results for growth of InAs/GaAs substrate on SiO_2 patterned surface. The film has a very large lattice mismatch with the substrate (~7%), which causes a large

compressive stress σ_{xx} in the film. The initial yield strength of InAs is assumed to be 2.5 GPa[58], which leads to an instantaneous yielding in the film. Relatively large plastic strain (~3%) throughout the entire flat film reduces the elastic strain ε_{xx} and subsequently stress σ_{xx}. Hence the ATGS instability is suppressed in the film as shown in Figs. 7(a)-(b). However, high interfacial energy between the film and the walls generates instabilities near the walls shown in Fig. 7(b). These instabilities start to grow and form islands due to the effects of the overflow deposition flux (Figs. 7(c)-(d)). Due to the high misfit strain, we find that the plastic deformation extends throughout the entire flat film and throughout the entire islands. Maximum plastic strain measured at a given time increases from 3% after 1×10^2 to 7% after 0.1 s. Experimental growth of InAs on GaAs substrates in 0.6μm wide trenches with deposition flux of 1 nm/s revealed formation of random islands across the pattern while these islands coalesce and form a single nucleus[16] during growth in addition to small islands witch exist near the walls in some cases. Our results for high In concentration alloys which are done under growth conditions similar to the experiments (e.g. growth temperature, flux rate, width of the pattern) are in a qualitative agreement with experimental studies by Ganesan *et al.* [16] on InAs/GaAs systems where the randomly nucleated islands across the pattern coalesce to form a single nucleus inside the pattern.

In Table III, we compare energetics for $In_xGa_{1-x}As/GaAs$ systems for x = 0.5, 0.75 and 1 after 0.1 s. The morphologies for x=0.5 and x=1 can be found in in Figs. (5), and (7), respectively. As shown in the last row of Table III, the total energy increases due to the increase in In concentration. This energy includes contributions from elastic, plastic, and interfacial energies. Higher In concentration causes a higher lattice mismatch and subsequently a higher stress in the film. Since the yield strength decreases when In concentration increases[58], higher plastic energy is expected for higher In concentration alloys. The plastic energy per unit length at a specific time for $In_{0.5}Ga_{0.5}As$ is 0.01×10^{-8} J/m while it is substantially higher (16.18×10^{-8} J/m) for InAs at the same time. It may be intuitive to expect an increasing trend for elastic energy per unit length with increasing In concentration. However, our results show that the elastic strain energy for InAs is 16.35×10^{-8} J/m is actually slightly smaller than the value found for $In_{0.75}Ga_{0.25}As$ (16.61×10^{-8} J/m). The decrease in elastic energy for larger In concentration can be attributed to large plastic deformation that occurred in the entire film and relaxes the accumulated elastic energy. For InAs film grown of GaAs this energy relaxation is large enough so that the film does not form ATGS instabilities.

Comparing the surface and interfacial energies in Table III, one can see a 4% increase between $In_{0.75}Ga_{0.25}As$ and InAs. The interface energy is zero since there is no contact between film and the walls. Hence this difference can be explained by the surface energy (the energy between the film and the gas phases) that has two contributions, one from free energy density function $f(c)$, and the other one from the gradient energy term $\frac{\varepsilon^2}{2}|\nabla c|^2$. Although the gradient energy coefficient (ε^2) decreases by increasing In concentration as shown in Table I and hence the gradient energy contribution to the surface energy is reduced, the surface energy increases due to increase in free energy density. The same increasing trend in surface and interfacial energy is observed between $In_{0.5}Ga_{0.5}As$ and $In_{0.75}Ga_{0.25}As$.

Table III. Energy comparison for $In_xGa_{1-x}As$ thin films (x = 0.5, 0.75 and 1) grown on GaAs. Surface energy refers to the energy of the film surface in contact with the gas phase, which has two contributions, one from free energy density and the other one from gradient energy. Interface energy refers to the energy between film and the walls.

Composition	$In_{0.5}Ga_{0.5}As$	$In_{0.75}Ga_{0.75}As$	InAs
Surface and interface energy (10^{-8} J/m)	39.74	41.81	43.6
Strain energy (10^{-8} J/m)	11.08	16.61	16.35
Plastic energy (10^{-8} J/m)	0.01	5.24	16.18
Total (elastic + plastic + interfacial) energy (10^{-8} J/m)	50.83	63.66	76.13

IV. CONCLUSIONS

We developed a phase field model coupled with elastoplasticity to study the effects of sub-micron sized patterns on morphology of heteroepitaxial films grown on patterned substrates. Our model considers the effects of anisotropy in elastic properties, non-uniform deposition flux and anisotropy in surface energy (between film and gas). To investigate the effect of lattice mismatch between the film and substrate on morphology we performed all the simulations under effects of biased deposition flux, which is observed in experiments. Diffusion coefficients, growth conditions, elastic constants, yield strengths, surface energies and lattice mismatch were chosen to correspond to the typical growth conditions of $In_xGa_{1-x}As$ thin films on GaAs substrates patterned with SiO_2.

Our results showed that there is a competition between overflow flux, surface diffusivity, strain energy and plastic relaxation on formation of islands in SiO_2 patterned GaAs substrates. For $In_xGa_{1-x}As$ alloys with low indium concentration (x smaller than 0.4) islands are formed at the walls mainly due to effects of

overflow flux while strain energy and surface diffusivity are relatively low because of low In concentration. There is no plastic deformation happening in this regime of concentrations. On the other hand, for $In_xGa_{1-x}As$ alloys with higher indium concentration (x larger than 0.4), surface diffusivity competes with the effect of the overflow flux to make a single island usually away from the walls. Elastic strain energy, which now has a higher value due to a higher lattice mismatch, is minimized by formation of a single island due to smaller area of strained interface. Plastic deformation partially relaxes strain energy of the island, which further reduces the motivation of the island to move. For In concentrations between 0.4 and 0.6 ($0.4 < x < 0.6$), plastic deformation only happens at the corners of the islands while for higher In concentration ($0.6 < x < 1$) the yielded region expands to the entire thin film and the islands. Also, the ATGS surface instability is suppressed for case of $x = 1$.

ACKNOWLEDGEMENTS

This research was primarily supported by University of Wisconsin Materials Research Science and Engineering Center (DMR-1121288). The authors also gratefully acknowledge the use of facilities and instrumentation supported by this grant and thank T. Kuech from the University of Wisconsin for helpful discussions.

REFERENCES

[1]S. Kohmoto, T. Ishikawa and K. Asakawa, *Japanese Journal Of Applied Physics*, **38**, 769, (1999).
[2]J. Hu, L.-S. Li, W. Yang, L. Manna, L.-W. Wang and A. P. Alivisatos, *Science*, **292**, 2060, (2001).
[3]A. Lorke, R. J. Luyken, A. O. Govorov and J. P. Kotthaus, *Physical Review Letters*, **84**, 2223, (2000).
[4]Y. Lei, W. Cai and G. Wilde, *Progress in Materials Science*, **52**, 465, (2007).
[5]G. M. Whitesides and B. Grzybowski, *Science*, **295**, 2418, (2002).
[6]S. B. Clendenning, S. Aouba, M. S. Rayat, D. Grozea, J. B. Sorge, P. M. Brodersen, R. N. S. Sodhi, Z.-H. Lu, C. M. Yip, M. R. Freeman, H. E. Ruda and I. Manners, *Advanced Materials*, **16**, 215, (2004).
[7]S. Matsui and Y. Ochiai, *Nanotechnology*, **7**, 247, (1996).
[8]W. Chu, H. I. Smith and M. L. Schattenburg, *Applied Physics Letters*, **59**, 1641, (1991).
[9]S. Kramer, R. R. Fuierer and C. B. Gorman, *Chemical Reviews*, **103**, 4367, (2003).
[10]D. Y. Ryu, K. Shin, E. Drockenmuller, C. J. Hawker and T. P. Russell, *Science*, **308**, 236, (2005).
[11]S. Jha, C.-C. Liu, T. S. Kuan, S. E. Babcock, P. F. Nealey, J. H. Park, L. J. Mawst and T. F. Kuech, *Applied Physics Letters*, 062104, (2009).
[12]G. Brammertza, M. R. Caymax, Y. Mols, S. Degroote, M. Leys, J. V. Steenbergen, G. Winderickx, G. Borghs and M. M. Meurisd, *ECS Transactions*, **3**, 585, (2006).
[13]J. Martin-Sanchez, P. Alonso-Gonzalez, J. Herranz, Y. Gonzalez and L. Gonzalez, *Nanotechnology*, **20**, 125302, (2009).
[14]V. C. Elarde, T. S. Yeoh, R. Rangarajan and J. J. Coleman, *Journal Of Crystal Growth*, **272**, 148, (2004).
[15]M. D. Takuya Hoshii, Masakazu Sugiyama, Ryosho Nakane, Satoshi Sugahara, Mitsuru Takenaka, Yoshika Nakano, and Shinichi Takagi, *Physical Status Solidus C*, **5**, 2733, (2008).
[16]S. Ganesan, University of Wisconsin – Madison, 2006.
[17]Z. R. Zytkiewicz, J. Domagala, D. Dobosz and J. Bak-Misiuk, *Journal Of Applied Physics*, **86**, 1965, (1999).

[18]K. Brunner, *Reports On Progress In Physics*, **65**, 93942, (2002).
[19]E. Jiran and C. Thompson, *Thin Solid Films*, 23, (1992).
[20]A. Boyne, M. D. Rauscher, S. A. Dregia and Y. Wang, *Scripta Materialia*, 705, (2011).
[21]R. J. Asaro and W. A. Tiller, *Metallurgical Transactions* **3**, 1789, (1972).
[22]M. A. Grinfeld, *Doklady Akademii Nauk SSSR* 1358, (1986).
[23]D. J. Srolovitz, *Acta Metallurgica*, **37**, 624, (1989).
[24]H. J. Gao and W. D. Nix, *Annual Review of Materials Science*, **29**, (1999).
[25]C. S. Ozkan, W. D. Nix and H. J. Gao, *Applied Physics Letters*, **70**, (1997).
[26]A. G. Cullis, A. J. Pidduck and M. T. Emeny, *Physical Review Letters*, **75**, (1995).
[27]J. Tersoff and F. K. Legoues, *Physical Review Letters*, **72**, (1994).
[28]D. E. Jesson, S. J. Pennycook, J. M. Baribeau and D. C. Houghton, *Physical Review Letters*, **71**, (1993).
[29]P. Kratzer, E. Penev and M. Scheffler, *Applied Surface Science*, **216**, 436, (2003).
[30]X. Su, R. K. Kalia, A. Nakano, P. Vashishta and A. Madhukar, *Applied Physics Letters*, **79**, 4577, (2001).
[31]T. P. Schulze and P. Smereka, *Communications in Computational Physics*, 1, (2010).
[32]B. J. Spencer, P. W. Voorhees and J. Tersoff, *Physical Review Letters*, **84**, 2449, (2000).
[33]J. Tersoff, *Physical Review Letters*, **87**, 156101, (2001).
[34]J. J. Eggleston, NORTHWESTERN UNIVERSITY, 2001.
[35]N. Moelans, B. Blanpain and P. Wollants, *Computer Coupling of Phase Diagrams and Thermochemistry*, **32**, 268, (2008).
[36]K. Thornton, J. Agren and P. W. Voorhees, *Acta Materiallia*, **51**, 5675, (2003).
[37]S. M. Wise and W. C. Johnson, *Journal Of Applied Physics*, 889, (2003).
[38]Y. Tu and J. Tersoff, *Physical Review Letters*, **98**, 096103, (2007).
[39]Y. Tu and J. Tersoff, *Physical Review Letters*, **93**, 216101, (2004).
[40]L.-Q. Chen, *Annual Review of Materials Research*, **August 2002**, 113, (2002).
[41]K. Kassner and C. Misbah, *Europhysics Letters*, 217, (1999).
[42]J. Drucker, *Physical Review B*, **48**, 18203, (1993).
[43]D. J. Seol, S. Y. Hu, Z. K. Liu, L. Q. Chen, S. G. Kim and K. H. Oh, *Journal Of Applied Physics*, 044910, (2005).
[44]D.-H. Yeon, P.-R. Cha and M. Grant, *Acta Materiallia*, **54**, 1623, (2006).
[45]B. J. Spencer, P. W. Voorhees and J. Tersoff, *Physical Review B*, **64**, 235318, (2001).
[46]S. M. Wise, J. S. Lowengrub, J. S. Kim and W. C. Johnson, *Superlattices And Microstructures*, 293, (2004).
[47]Y. U. Wang, Y. M. Jin, A. M. Cuitino and A. G. Khachaturyan, *Acta Materialia*, **49**, (2001).
[48]Y. U. Wang, Y. M. Jin, A. M. Cuitino and A. G. Khachaturyan, *Applied Physics Letters*, **78**, (2001).
[49]M. Haataja, J. Muller, A. D. Rutenberg and M. Grant, *Physical Review B*, **65**, (2002).
[50]M. Haataja, J. Muller, A. D. Rutenberg and M. Grant, *Physical Review B*, **65**, (2002).
[51]Y. U. Wang, Y. M. M. Jin and A. G. Khachaturyan, *Acta Materialia*, **51**, (2003).
[52]M. Cottura, Y. Le Bouar, A. Finel, B. Appolaire, K. Ammar and S. Forest, *Journal of the Mechanics and Physics of Solids*, **60**, (2012).
[53]X. H. Guo, S. Q. Shi and X. Q. Ma, *Applied Physics Letters*, **87**, (2005).
[54]A. Gaubert, Y. Le Bouar and A. Finel, *Philosophical Magazine*, **90**, (2010).
[55]T. Nishinaga, *Journal Of Crystal Growth*, **237**, (2002).
[56]J. W. C. a. J. E. Hilliard, *Journal Of Chemical Physics*, **28**, 258, (1958).
[57]S. M. Allen and J. W. Cahn, *Acta Metallurgica*, **27**, 1085, (1979).
[58]S. Korte, I. Farrer and W. J. Clegg, *Journal of Physics D-Applied Physics*, **41**, (2008).
[59]J. W. Cahn, *Journal of chemical physics*, 3667, (1977).
[60]S. M. Wise, J. S. Kim and W. C. Johnson, *Thin Film Solids*, 151, (2005).
[61]J. W. Cahn, *Acta Metallurgica*, **9**, 795, (1967).
[62]E. Placidi, F. Arciprete, R. Magri, M. Rosini, A. Vinattieri, L. Cavigli, M. Gurioli, E. Giovine, L. Persichetti, M. Fanfoni, F. Patella and A. Balzarotti, in *Self-assembly of nanostructures: The infn lectures, vol. Iii, lecture notes in nanoscale science and technology 12, doi 10.1007/978-1-4614-0742-3_2, # springer science+business media, llc 2012*, edited by Springer (2012).
[63]M. Kasu and N. Kobayashi, *Journal Of Crystal Growth*, **145**, 120, (1994).
[64]M. Rosini, M. C. Righi, P. Kratzer and R. Magri, *Physical Review B*, 075302, (2009).
[65]H. Ye, Z. Y. Yu, P. F. Lu, Y. M. Liu and L. H. Han, *Journal Of Applied Physics*, **114**, (2013).
[66]R. Gatti, A. Marzegalli, V. A. Zinovyev, F. Montalenti and L. Miglio, *Physical Review B*, **78**, (2008).
[67]X. D. Liang, Y. Ni and L. H. He, *Computational Materials Science*, **48**, (2010).

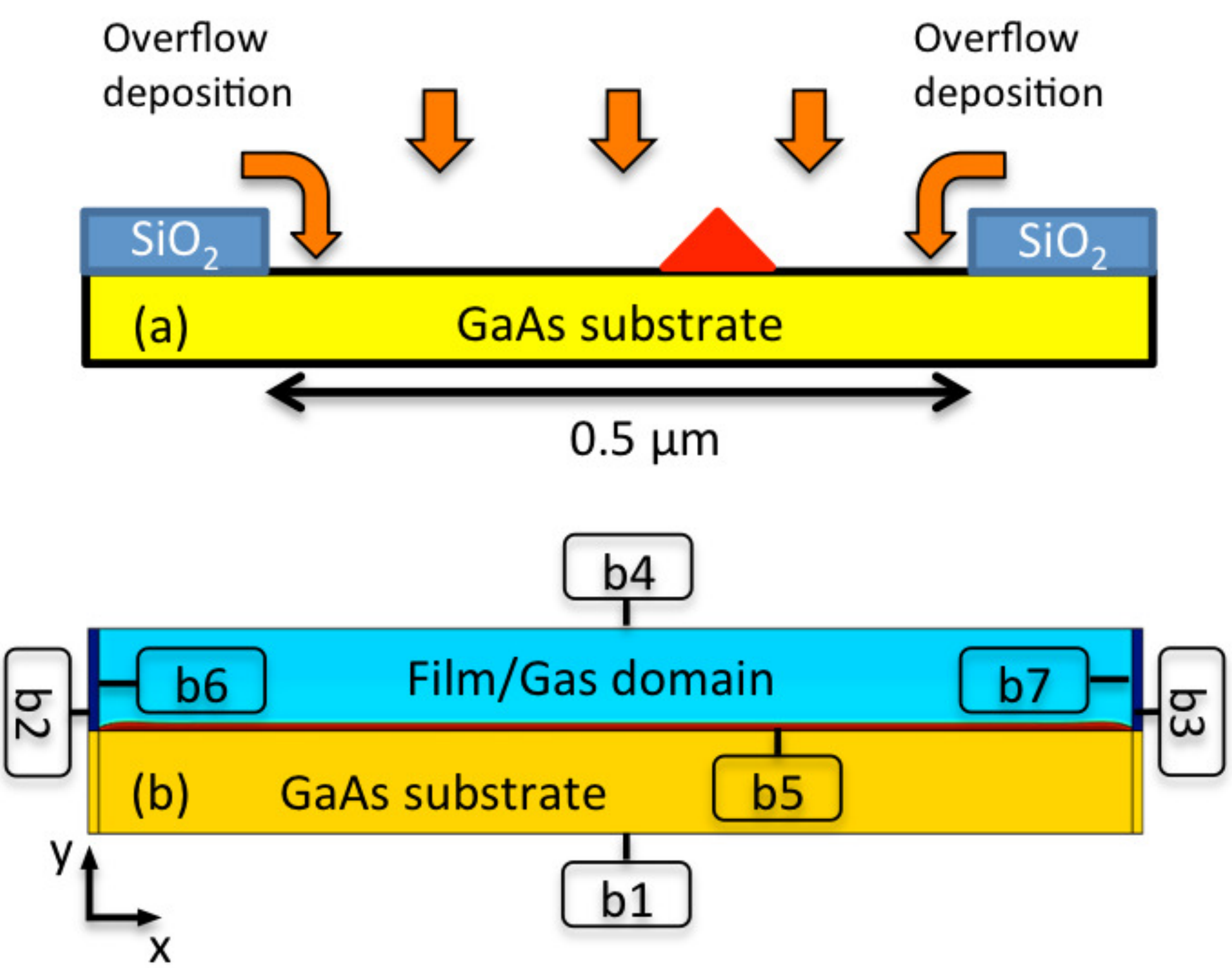
Overflow deposition
Overflow deposition
SiO2
SiO2
(a)
GaAs substrate
0.5 µm
b4
b6
Film/Gas domain
b7
b2
b3
(b)
GaAs substrate
b5
b1
y
x

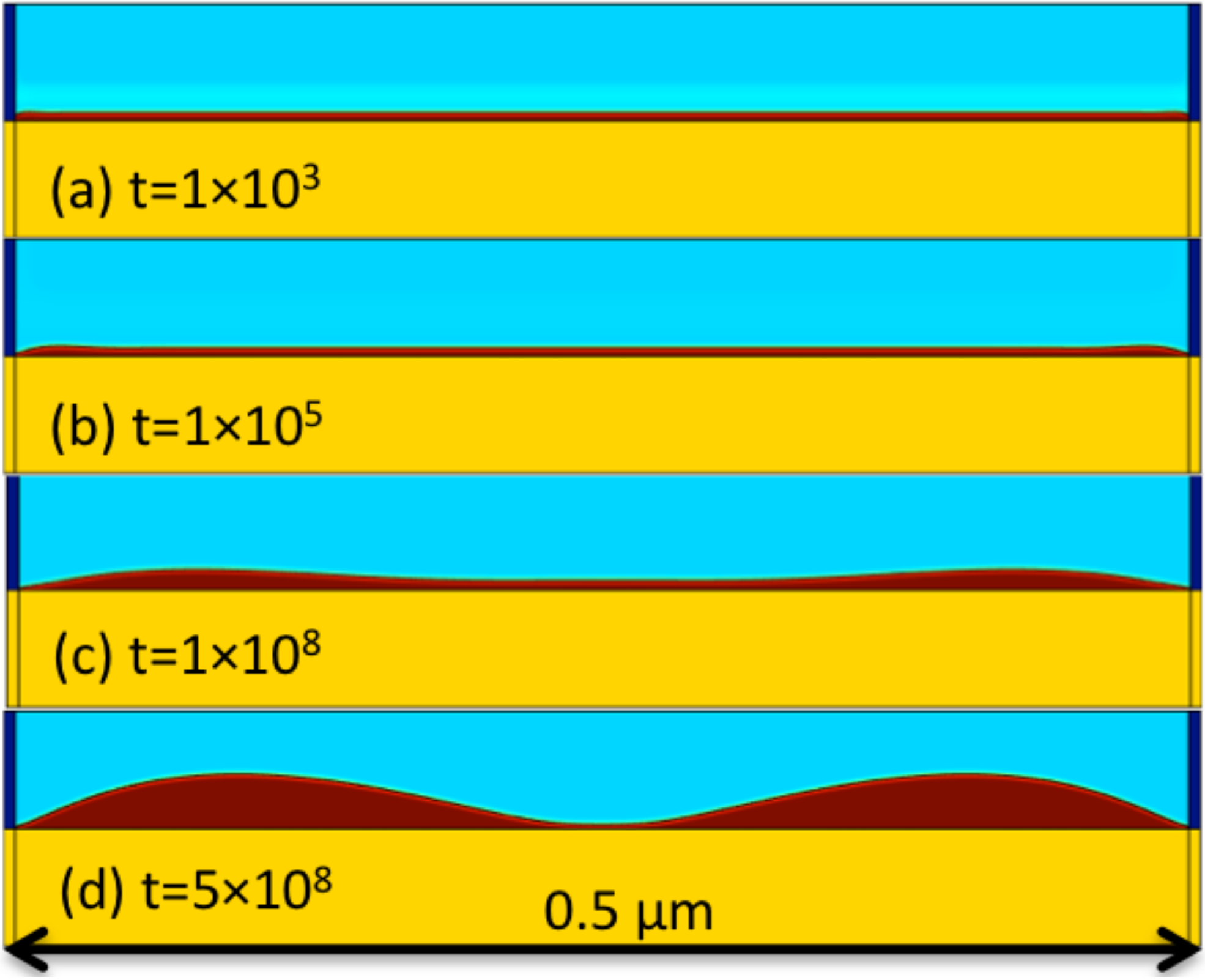
(a) t=1×10^3
(b) t=1×10^5
(c) t=1×10^8
(d) t=5×10^8
0.5 μm

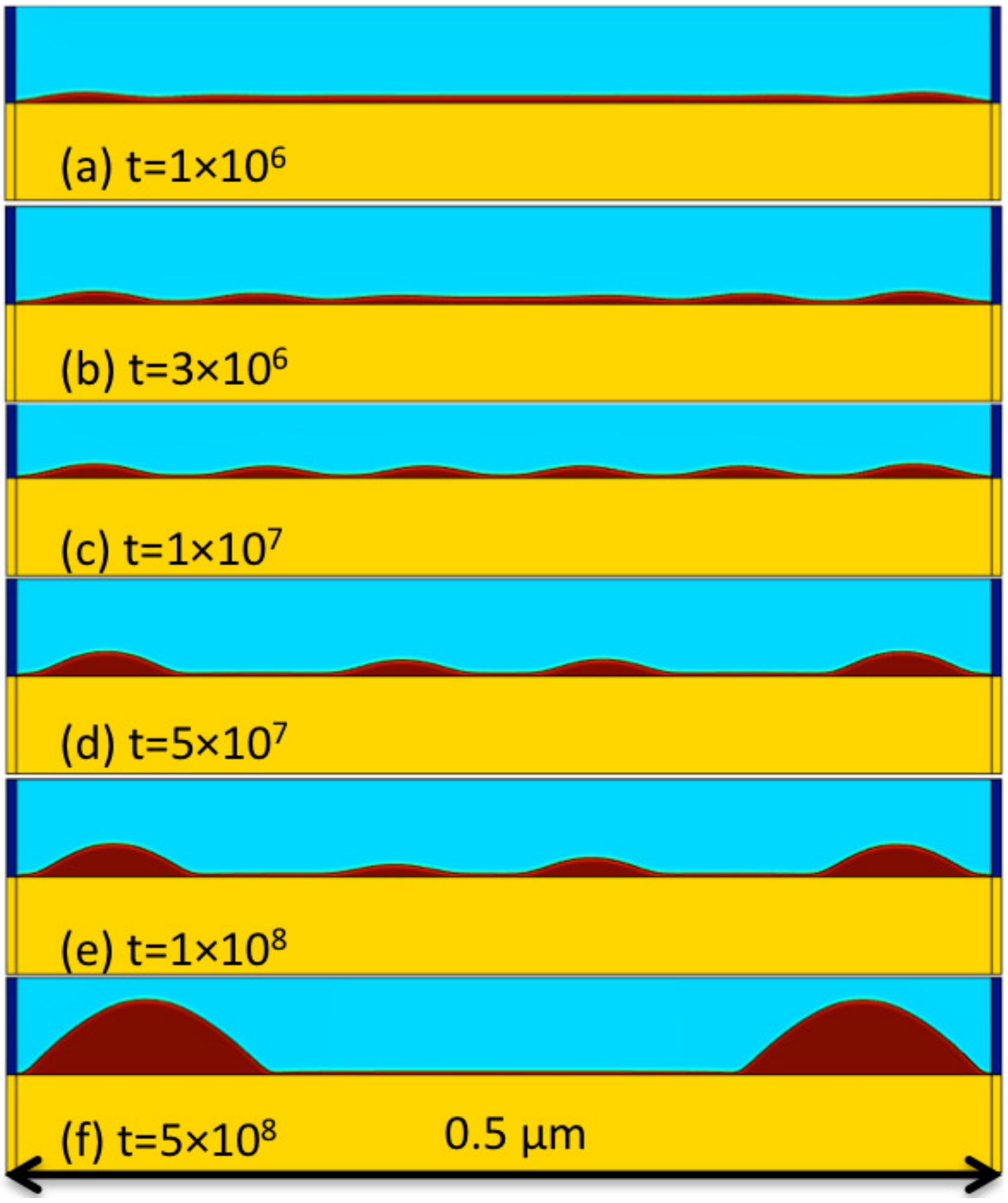
(a) t=1×10^6
(b) t=3×10^6
(c) t=1×10^7
(d) t=5×10^7
(e) t=1×10^8
(f) t=5×10^8
0.5 μm

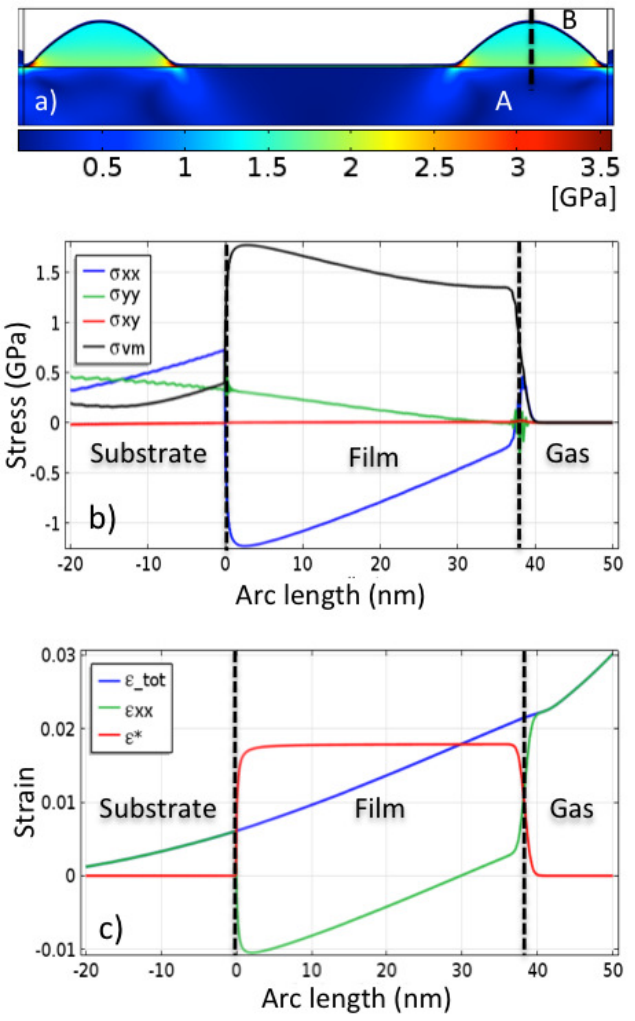
B
a)
A
0.5
1
1.5
2
2.5
3
3.5
[GPa]
σxx
σyy
σxy
σvm
Stress (GPa)
Substrate
Film
Gas
b)
Arc length (nm)
ε_tot
εxx
ε*
Strain
Substrate
Film
Gas
c)
Arc length (nm)

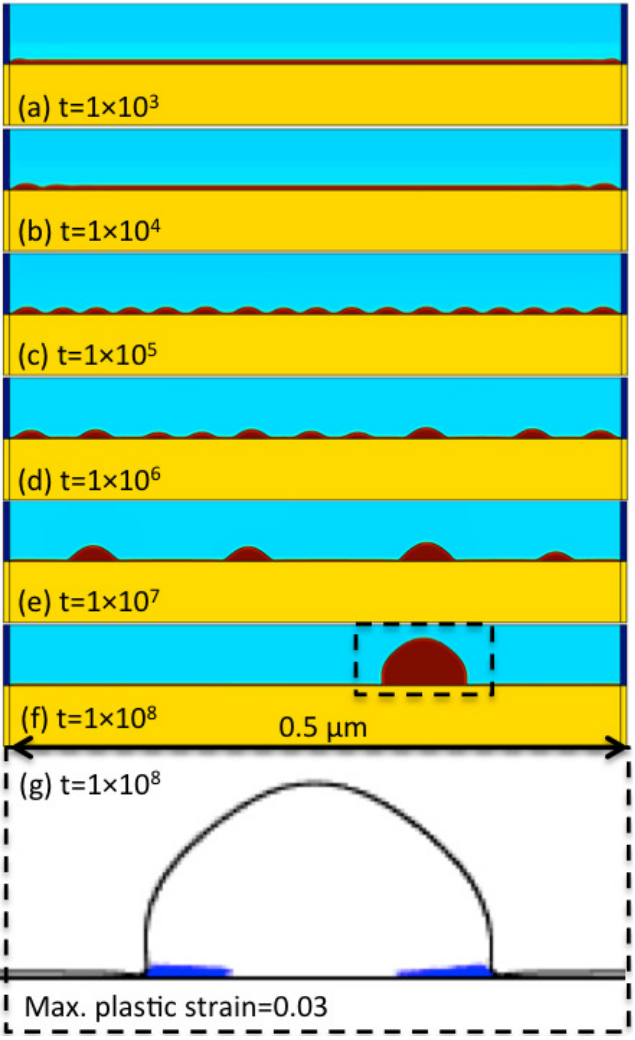
(a) t=1×10^3
(b) t=1×10^4
(c) t=1×10^5
(d) t=1×10^6
(e) t=1×10^7
(f) t=1×10^8
0.5 μm
(g) t=1×10^8
Max. plastic strain=0.03

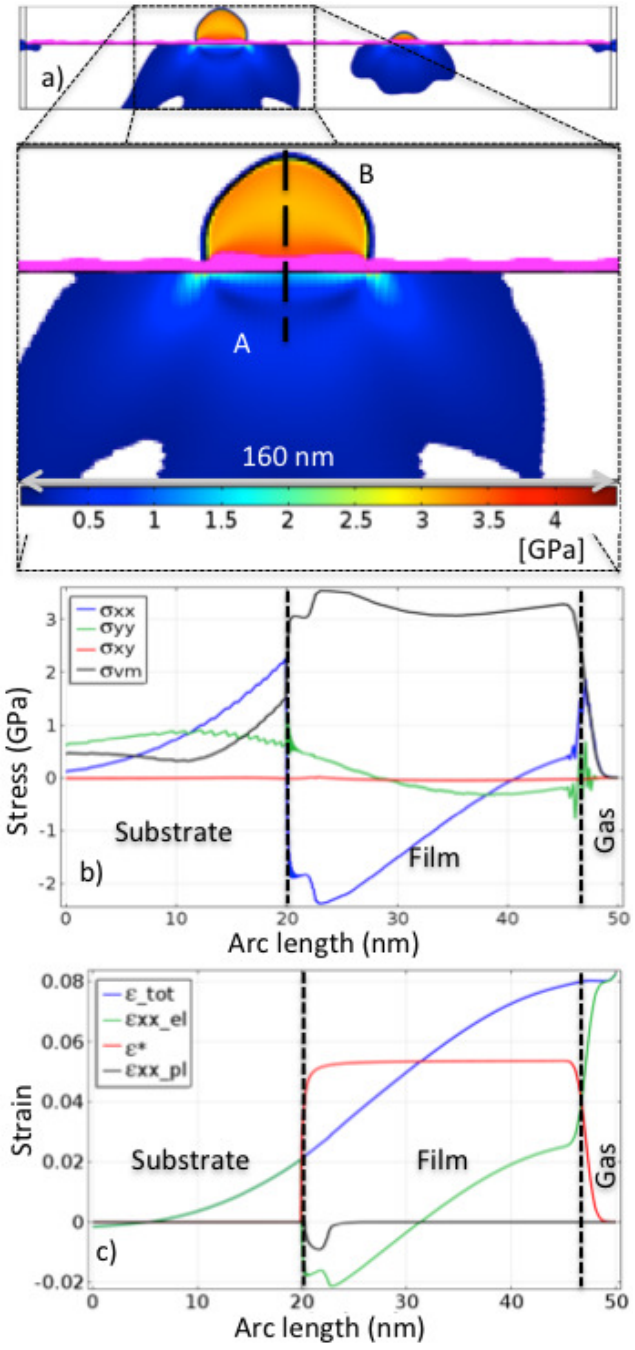
a)
B
A
160 nm
0.5
1
1.5
2
2.5
3
3.5
4
[GPa]
σxx
σyy
σxy
σvm
Stress (GPa)
Substrate
Film
Gas
b)
Arc length (nm)
ε_tot
εxx_el
ε*
εxx_pl
Strain
Substrate
Film
Gas
c)
Arc length (nm)

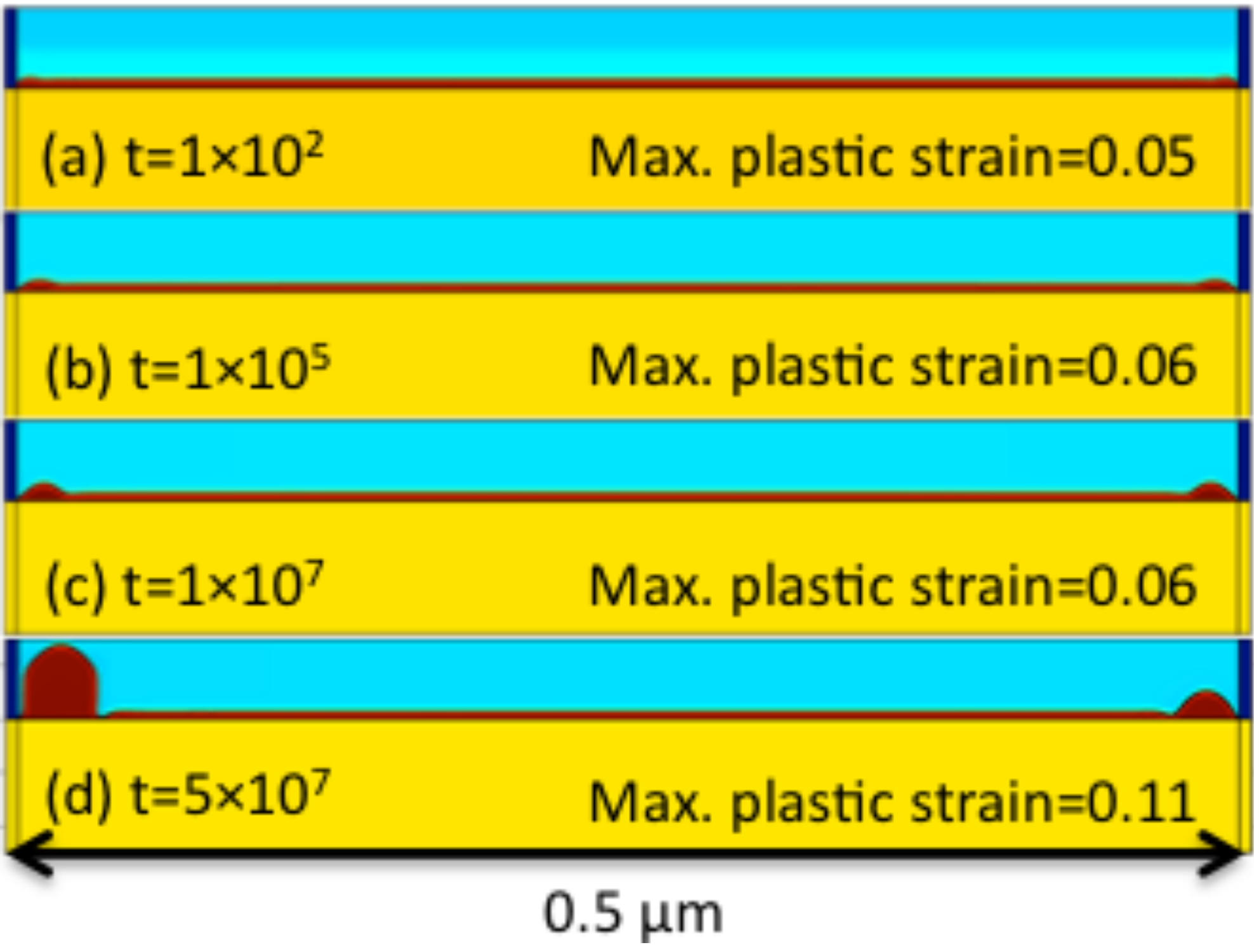
(a) t=1×10^2
Max. plastic strain=0.05
(b) t=1×10^5
Max. plastic strain=0.06
(c) t=1×10^7
Max. plastic strain=0.06
(d) t=5×10^7
Max. plastic strain=0.11
0.5 μm